# Chapter 3

# Beam Dynamics issues

## 3.1 Beam-beam interaction

### 3.1.1 Introduction

SuperKEKB is designed with the strategy of so-called the nano beam scheme. Electron-positron beams collide with a horizontal crossing angle of $2\phi_c = 2 \times 41.5$ mrad. The beam sizes at the interaction point (IP) are $\sigma_{x+} = 10$ $\mu$m and $\sigma_{x-} = 11$ $\mu$m for positron and electron beams, respectively. The overlap area of the two beam is $\Delta s = \sigma_x/\phi_c \simeq$ 0.25 mm. The area is 1/20-1/25 of the bunch length, since the bunch lengths are $\sigma_{z+} = 6$ mm and $\sigma_{z-} = 5$ mm. Figure 3.1 sketches out the collision, when the central parts of a pair of bunches collide. The beams travel along $s$ to the opposite direction for electron and positron. The parallel translation along the $x$ direction for the two beams is neglected in this picture.
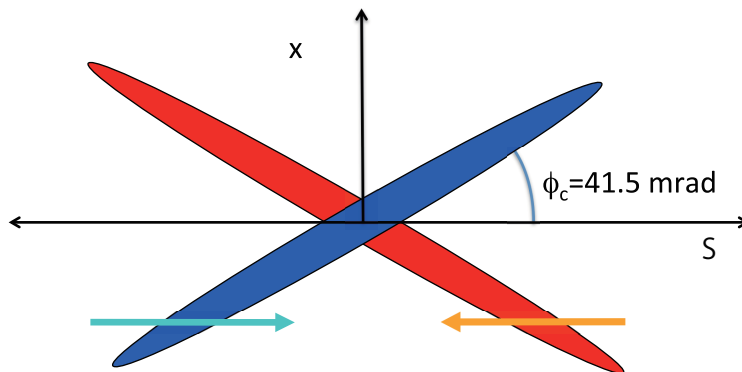


Figure 3.1: Schematic view of nano-beam collision.

Another characteristic of SuperKEKB is the small vertical beta function $(\beta_y^*)$ at the IP. The beta function is squeezed to be $\beta_{y+} = 0.27$ mm and $\beta_{y-} = 0.30$ mm since

the overlap area is very small size of 0.25 mm.

The vertical emittances are assumed to be $\varepsilon_{y+} = 8.64$ pm, $\varepsilon_{y-} = 12.9$ pm with taking into account of the beam-beam interaction. The design luminosity for 2500 bunches is $8 \times 10^{35}$ cm$^{-2}$ s$^{-1}$.

The tune shifts due to the beam-beam collision are $\xi_{x/y+} = 0.0028/0.0881$, $\xi_{x/y-} = 0.0012/0.0807$ for positrons and electrons, respectively, with $z = 0$. The horizontal tune shift is small, because of the large projected beam size $\Sigma_x = \sqrt{(\sigma_{z-}\phi_c)^2 + (\sigma_{z+}\phi_c)^2}$.

The luminosity performance is evaluated by a weak-strong beam-beam simulation. In the weak-strong simulation, one (weak) beam is expressed by many (macro)-particles, and other (strong) beam is assumed to be a fixed Gaussian charge distribution. As shown in later, the positron beam easily enlarges compared to the electron beam. The positron and electron beams are treated as the weak and strong beams, respectively, in the most of this report.

The weak beam, which is Gaussian distribution initially, is generated by random variables. The horizontal emittances are $\varepsilon_{x+} = 3.2$ nm and $\varepsilon_{x-} = 4.6$ nm with taking into account of the intrabeam effect.

The vertical emittance of the weak beam are initialized with $\varepsilon_y = 4.7$pm(e$^+$) or 1.6 pm(e$^-$), since x-y coupling at zero current is $\kappa_+ = 0.05\%$ and $\kappa_- = 0.23\%$.

Macro particles in the weak beam are tracked during many turns with a transformation along arc section and the beam-beam interaction with the strong beam. The luminosity performance is evaluated after the equilibrium for the beam-beam interaction, radiation damping and excitation.

The revolution of the beam along arc section is expressed by a transformation using $6 \times 6$ matrix $(M)$ in this subsection. The revolution matrix is represented by the eigenvalues and eigenvectors.

$$M = VUV^{-1} \qquad V = R_\eta RB \tag{3.1}$$

The block diagonalized matrix $(U)$ is represented by the tunes $(\nu_x, \nu_y, \nu_z)$.

$$U = \begin{pmatrix} U_x & 0 & 0 \\ 0 & U_y & 0 \\ 0 & 0 & U_z \end{pmatrix} \qquad U_i = \begin{pmatrix} \cos\mu_i & \sin\mu_i \\ -\sin\mu_i & \cos\mu_i \end{pmatrix} \tag{3.2}$$

where $\mu_i = 2\pi\nu_i$.

The eigenvectors are parametrized by the matrices, $R_\eta$, $R$ and $B$.

$$R_\eta = \begin{pmatrix} \{1 - |R_{\eta,x}|/(1+r_{\eta,0})\}I_2 & R_{\eta,x}S_2 R_{\eta,y}^T S_2/(1+r_{\eta,0}) & R_{\eta,x} \\ R_{\eta,y}S_2 R_{\eta,x}^T S_2/(1+r_{\eta,0}) & \{1 - |R_{\eta,y}|/(1+r_{\eta,0})\}I_2 & R_{\eta,y} \\ S_2 R_{\eta,x}^T S_2 & S_2 R_{\eta,y}^T S_2 & r_{\eta,0}I_2 \end{pmatrix}, \tag{3.3}$$

where $R_{\eta,x}$, $R_{\eta,y}$, $S_2$, and $I_2$ are $2 \times 2$ matrices:

$$R_{\eta,i} = \begin{pmatrix} \zeta_i & \eta_i \\ \zeta_i' & \eta_i' \end{pmatrix} \qquad i = x, y, \tag{3.4}$$

$$S_2 = \begin{pmatrix} 0 & 1 \\ -1 & 0 \end{pmatrix} \qquad I_2 = \begin{pmatrix} 1 & 0 \\ 0 & 1 \end{pmatrix}, \tag{3.5}$$

$r_{\eta,0} = \sqrt{1 - |R_{\eta,x}| - |R_{\eta,y}|}$. $\zeta$'s are induced by crab cavities. Such a transverse deflecting component is very weak in ordinary accelerators, thus $\zeta$'s $= 0$, $r_{\eta,0} = 1$ in this report.

$$R = \begin{pmatrix} r_0 I_2 & -S_2 R_2^T S_2 & 0 \\ -R_2 & r_0 I_2 & 0 \\ 0 & 0 & I_2 \end{pmatrix} \qquad R_2 = \begin{pmatrix} r_1 & r_2 \\ r_3 & r_4 \end{pmatrix}, \tag{3.6}$$

where $r_0 = \sqrt{1 - |R_2|}$.

$$B = \begin{pmatrix} B_x & 0 & 0 \\ 0 & B_y & 0 \\ 0 & 0 & B_z \end{pmatrix} \qquad B_i = \begin{pmatrix} \frac{1}{\sqrt{\beta_i}} & 0 \\ \frac{\alpha_x}{\sqrt{\beta_i}} & \sqrt{\beta_i} \end{pmatrix} \tag{3.7}$$

The weak beam particles are transferred before and after beam-beam interaction effectively due to the crossing angle. The particles are transferred before collision as follows,

$$\begin{aligned}
x^* &= \tan\theta z + \left(1 + \frac{p_x^*}{p_s^*}\sin\theta\right)x \\
y^* &= y + \sin\theta \frac{p_y^*}{p_s^*}x \\
z^* &= \frac{z}{\cos\theta} - \frac{H^*}{p_s^*}\sin\theta x \\
p_x^* &= \frac{p_x - \tan\theta H}{\cos\theta} \\
p_y^* &= \frac{p_y}{\cos\theta} \\
p_z^* &= p_z - \tan\theta p_x + \tan^2\theta H,
\end{aligned} \tag{3.8}$$

where

$$H = (1 + p_z) - \sqrt{(1 + p_z)^2 - p_x^2 - p_y^2}$$

$$p_s = \sqrt{(1 + p_z)^2 - p_x^2 - p_y^2}.$$

The particles are transferred after the collision with the inverse of Eq.(3.8).

42

The linear part of Eq.(3.8) is expressed by a matrix

$$
T_L = \begin{pmatrix}
1 & 0 & 0 & 0 & \tan\theta & 0 \\
0 & 1/\cos\theta & 0 & 0 & 0 & 0 \\
0 & 0 & 1 & 0 & 0 & 0 \\
0 & 0 & 0 & 1/\cos\theta & 0 & 0 \\
0 & 0 & 0 & 0 & 1/\cos\theta & 0 \\
0 & -\tan\theta & 0 & 0 & 0 & 1
\end{pmatrix}.
\tag{3.9}
$$

This matrix transformation performs $x - z$ tilt as shown in Figure 3.1.

The strong beam is assumed to have a rigid Gaussian distribution in real 3 dimensional space. The electro-magnetic field of a point charge traveling the light speed is formed in the perpendicular plane to the traveling direction. The strong beam is sliced along the bunch length $z$. The electro-magnetic field of each slice depends on the charge in a slice of $\delta z$ and the distribution (Gaussian in x-y plane). The weak beam particles travel with the kick of electro-magnetic field and drift between slices. The kick, which a positron particle with a deviation of $(x, y)$ from the center of distribution experiences, is expressed by

$$
dp_y + i dp_x = \frac{2n_-(z)\delta z r_e}{\gamma} \sqrt{\frac{\pi}{2(\sigma_x^2 - \sigma_y^2)}} \times
$$

$$
\left[ w\left( \frac{x + iy}{\sqrt{2(\sigma_x^2 - \sigma_y^2)}} \right) - \exp\left( -\frac{x^2}{2\sigma_x^2} - \frac{y^2}{2\sigma_y^2} \right) w\left( \frac{\frac{\sigma_y}{\sigma_x}x + \frac{\sigma_x}{\sigma_y}y}{\sqrt{2(\sigma_x^2 - \sigma_y^2)}} \right) \right],
\tag{3.10}
$$

where $n_-(z_-)$ is the electron line density at $z_-$ and $w(x)$ is the complex error function.

In the revolution matrix (3.1), $\nu$ and $\beta$ is certain number but other 15 parameters are 0 in the design of SuperKEKB. $\beta_{x,y}$ is determined for the design luminosity. Choice of tune is discussed in 3.1.2 in detail.

Figure 3.2 shows the simulation result for the tune $\nu_x = 0.53, \nu_y = 0.58$, which was promised area in KEKB. Red curve plots luminosity and beam size evolution, in which the positron and electron beams are weak and strong, respectively. Blue curve plots them, in which the role of weak/strong is exchanged; weak electron and strong positron. Blue curve is higher than the design luminosity, while red curve just achieves the design luminosity in the equilibrium (after 2000 turns). The positron beam easily enlarges due to the interaction with the electron beam. The red curve is realistic case, because electron beam does not blow up. Emittance evolution, which is evaluated by the second order moment of the weak particles, is plotted in the right picture. The design luminosity is achieved even though emittance of positron beam is twice of the design. This fact means the core distribution is not enlarged so strongly. Hereafter

the case of the positron weak and electron strong beams is studied in the weak-strong simulation.
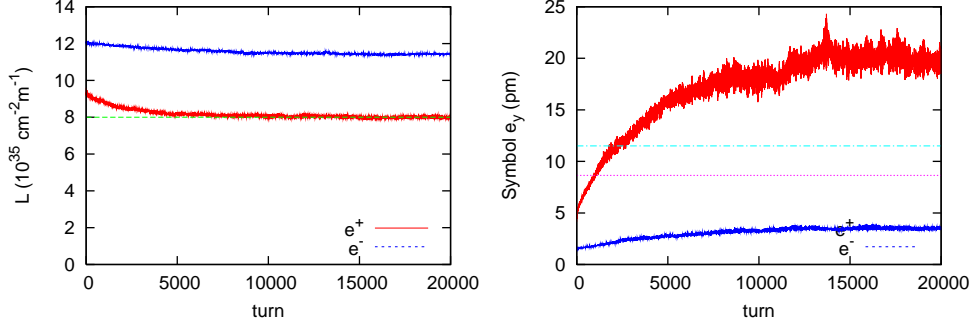


Figure 3.2: Luminosity and emittance evolution in the weak-strong simulation. Red line is given for weak positron and strong electron beams. Blue line is given for weak electron and strong positron beams. Cyan and magenta curves in the right picture are the design emittance of electron and positron beams, respectively.

## 3.1.2 Tune Scan

It is well known that high luminosity can be achieved at electron-positron colliders with working point chosen to be chose to be the half integer. To search for the best working point in the tune space, tune scans are performed for both LER and HER, with fractional tunes in the range of [0.50, 0.75] and the beam currents set to design values. The results of tune scans for the LER and HER are demonstrated in Fig. 3.3-3.5 with scaled colors. Figure 3.3 shows the results of luminosity scan, and Fig. 3.4 and 3.5 are the relevant scans of horizontal and vertical beam sizes. It is seen that the strong synchro-betatron resonances of $2\nu_x - N\nu_s = Integer$ exist in the nano-beam scheme. This is due to the large crossing angle chosen for the purpose of mitigating hourglass effects. Furthermore, the resonances of $\nu_x + 2\nu_y + N\nu_s = Integer$, $2\nu_y - \nu_s = Integer$, and $\nu_x - \nu_y - \nu_s = Integer$ also restrict the choice of working point. The working points have to be kept far enough from these strong resonances. In general, the luminosity is very sensitive to the vertical beam size. It is also observed that the electron beam in HER is more robust than the positron beam in LER with respect to the beam-beam driven synchro-betatron resonances. At present, both the main rings of the SuperKEKB are optimized with fractional tunes of (0.53, 0.57).

The effects of synchro-betatron resonances are more clearly seen in Fig. 3.6, where the scans of horizontal tune are done with fixed fractional vertical tune at 0.57. The red solid lines correspond to the results using the pure weak-strong model. The widths
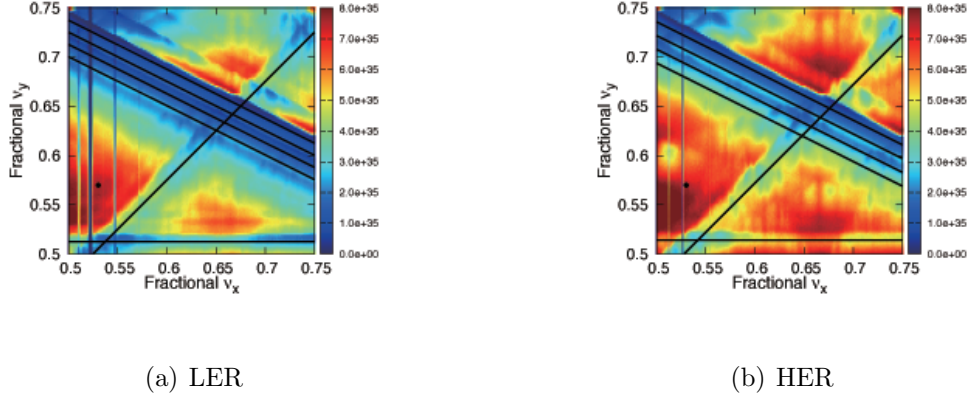
(a) LER

(b) HER

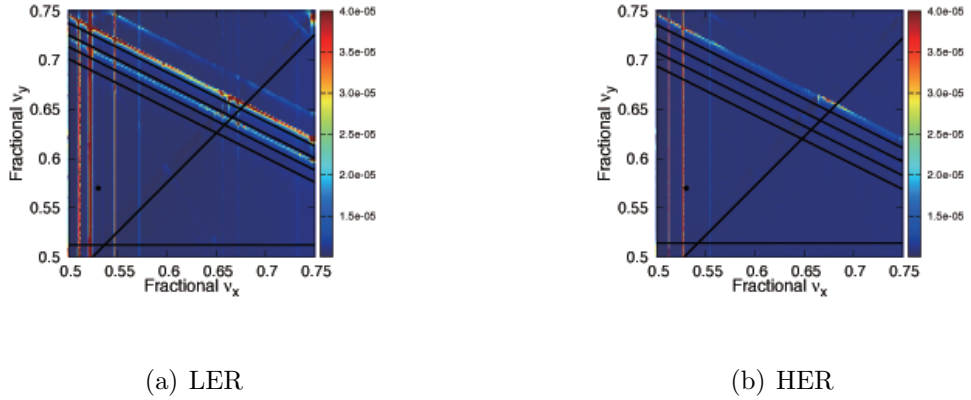Figure 3.3: Luminosity tune scans for the LER and HER.



(a) LER

(b) HER

Figure 3.4: Horizontal beam sizes with beam-beam for the LER and HER.

of resonances are narrower in the case of HER than in the case of LER. It implies that the high energy beam is relatively immune from beam-beam perturbation.

### 3.1.3 Errors of orbit at collision point

The luminosity degradation is caused by collision with an offset of the two beams. The geometrical luminosity loss with orbit offsets is given by

$$\frac{\Delta L}{L_0} = \exp\left(-\frac{\Delta x^2}{4\Sigma_x^2} - \frac{\Delta y^2}{4\Sigma_y^2}\right),\tag{3.11}$$
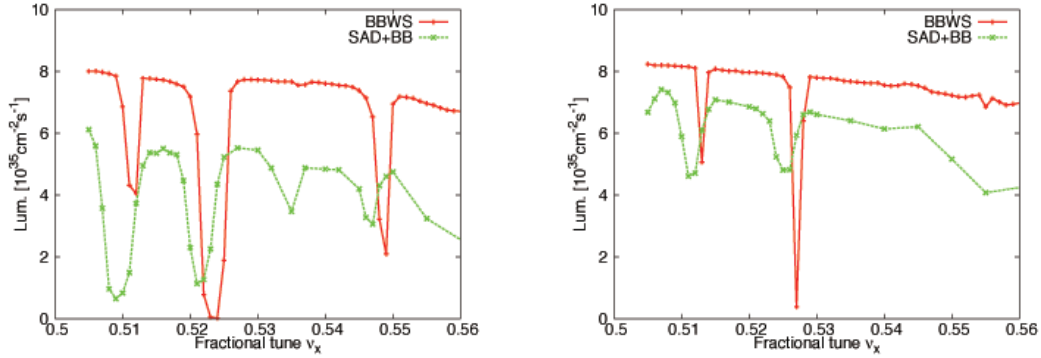
where the projected beam size $\Sigma_x = \sqrt{\sigma_x^2 + (\sigma_z \phi_c)^2}$, $\Sigma_y = \sigma_y$. Actually the luminosity degradation is stronger due to the dynamic effect of the beam-beam interaction. The luminosity degradation depends on whether the collision offset is static or fast (turn-by-turn) fluctuation.
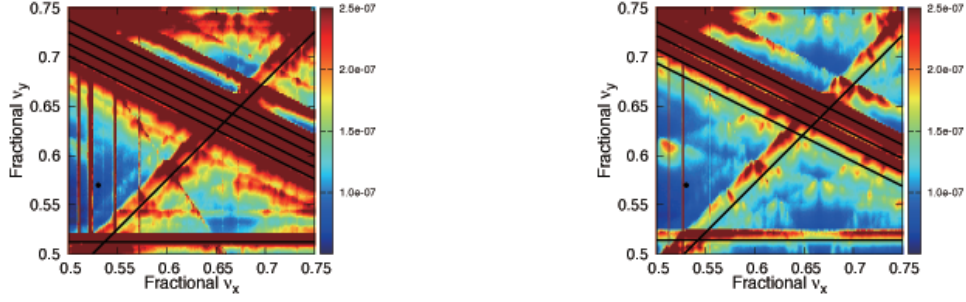
(a) LER

(b) HER

Figure 3.5: Vertical beam sizes with beam-beam for the LER and HER.



(a) LER

(b) HER

Figure 3.6: Total luminosity as a function of horizontal tune for LER and HER, with fractional vertical tune of 0.57.

**Static offset error**

To evaluate the effect of a static offset, the weak-strong simulation is performed with the strong beam shifted by $(\Delta x, \Delta y)$. For the nano-beam scheme, the contribution of bunch length is dominant in the horizontal projected beam size, $\Sigma_x \gg \sigma_x$. While the horizontal offset $\Delta x$ results a shift of overlap area $\Delta s$ as shown in Figure 3.7. Two beams collide with a shift of vertical waist. Therefore the sensitivity for horizontal offset is $\sigma_x$, but not $\Sigma_x$.

The equilibrium luminosity and vertical emittance are calculated for several offset values. Figure 3.8 shows the equilibrium luminosity and vertical beam size normalized by $L_0 = 8 \times 10^{35}$ cm$^{-2}$s$^{-1}$ and the design beam size $\sigma_{y,0}$. On the whole the luminosity degradation is quadratic for small errors. For 20% degradation, tolerable offset is 0.8 $\sigma_x$ and 0.8 $\sigma_y$ in horizontal and vertical, respectively.
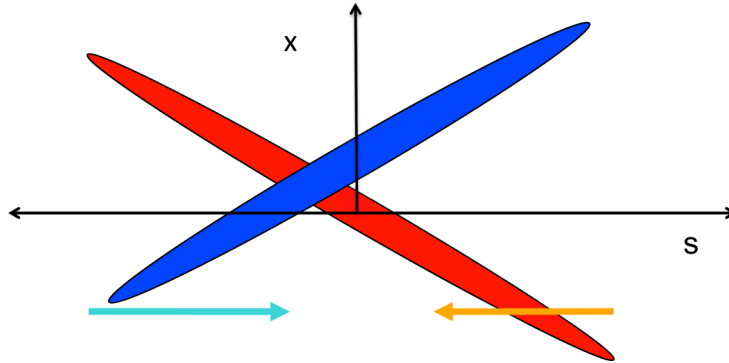
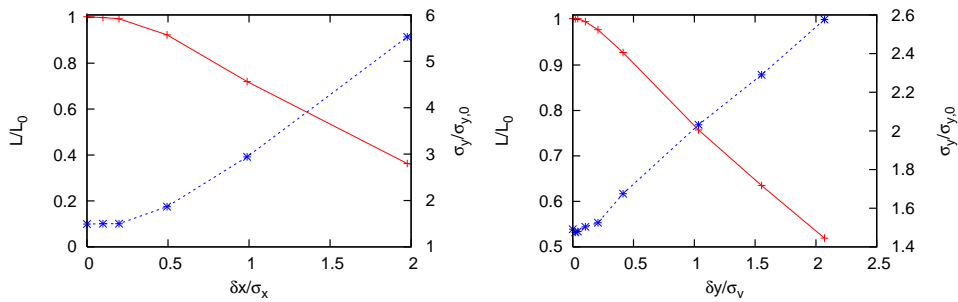Figure 3.7: nano-beam collision scheme.



Figure 3.8: Liminosity degradation for static collision offset. Left and right pictures depict the degradation for horizontal and vertical offset, respectively. Red and blue lines are luminosity and beam size, respectively.

**Turn-by-turn offset fluctuation**

In the weak-strong simulation, particles move in a given potential formed by colliding beam; Hamiltonian system. Fluctuation of collision offset results in fluctuation of the potential, which enhances emittance growth. Figure 3.9 shows the luminosity degradation for turn-by-turn offset fluctuation. For 20% degradation, tolerable offset is 0.08 $\sigma_x$ and 0.09 $\sigma_y$ in horizontal and vertical, respectively. The sensitivity is one order severer than that of static offset.
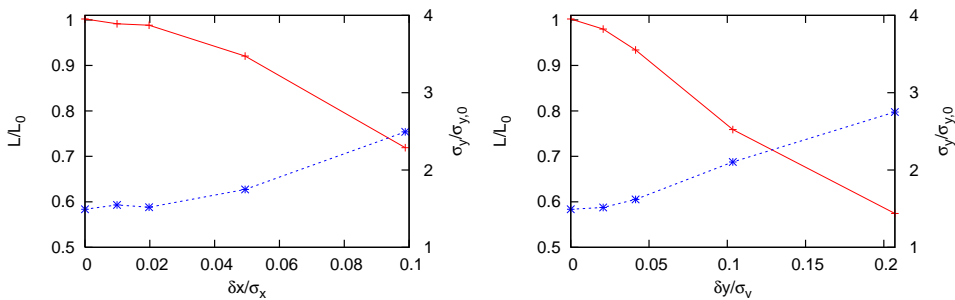


Figure 3.9: Liminosity and emittance degradations for turn-by-turn collision offset. Left and right pictures depict the degradations for horizontal and vertical offset, respectively. Red and blue lines are luminosity and beam size, respectively.

### 3.1.4 Error of linear optics parameters

Optics parameters at the IP which are zero in the design have nonzero values due to strength and alignment errors of magnets in a real accelerator. The nonzero values of the parameters break symmetry of the beam-beam force and cause emittance growth and luminosity degradation.

$\beta_x$ is larger than $\beta_y$ and $\sigma_z$. Therefore, the errors for $\beta_x$ and $\alpha_x$ should not be sensitive to the luminosity performance. Errors for $\beta_y$ and $\alpha_y$ are treated as a vertical waist shift in this report. The minimum beta is evaluated accurately by a measurement of $\beta_y$ at IR magnets, while it is ambiguous how the waist of $\beta_y$ shifts from the IP. Figure 3.10 shows the luminosity and emittance degradation due to the waist shift. For 20% degradation, tolerable waist shift is 0.07 mm. As is mentioned in Sec. 3.1.3, the waist error gives similar effect as the horizontal offset; $ds = \delta x / 2\phi_c$ is satisfied.

Luminosity degradation due to x-y coupling and dispersion at the IP is evaluated as shown in Figures 3.11 and 3.12. Small horizontal dispersion ($\eta_x \delta \ll \sigma_x$) should not
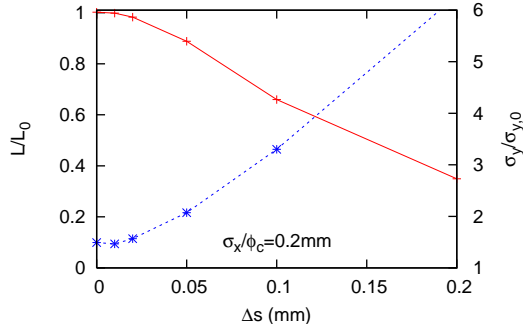
Figure 3.10: Luminosity and emittance degradations due to vertical waist error. Red and blue lines are luminosity and beam size respectively.

be serious.

### Chromatic aberrations for linear optics parameters

Chromatic aberrations of the optics parameters, $d\nu_{xy}/d\delta$, $d\beta_{x,y}/d\delta$ and $dr_i/d\delta$, affect the luminosity performance. The weak-strong simulations were performed to evaluate tolerance for the chromatic aberrations.

## 3.1.5   Summary for the error tolerance

The tolerance for the optics errors are summarized in Table 3.1.

## 3.1.6   Lattice nonlinearity

Beam-beam interaction may interplay with lattice nonlinearity and cause luminosity loss. To evaluate its effect, the SAD code [1] is utilized to do element-by-element tracking simulations with the beam-beam element inserted at the IP. The total one-turn map used in the simulations can be represented by

$$M = M_{rad} \circ M_{bb} \circ M_0, \tag{3.12}$$

where $M_{bb}$ and $M_{rad}$ are maps for the beam-beam interaction and radiation damping/quantum excitation, respectively. And $M_0$ indicates the transfer map felt by a particle when it travels through normal magnetic and electromagnetic components along the ring. The lattice nonlinearity is naturally included in $M_0$ when a realistic lattice is loaded in the SAD code.

Another method for the simulations with momentum-dependent lattice nonlinearity was discussed in Refs. [2, 3], where a symplectic formalism was developed to describe
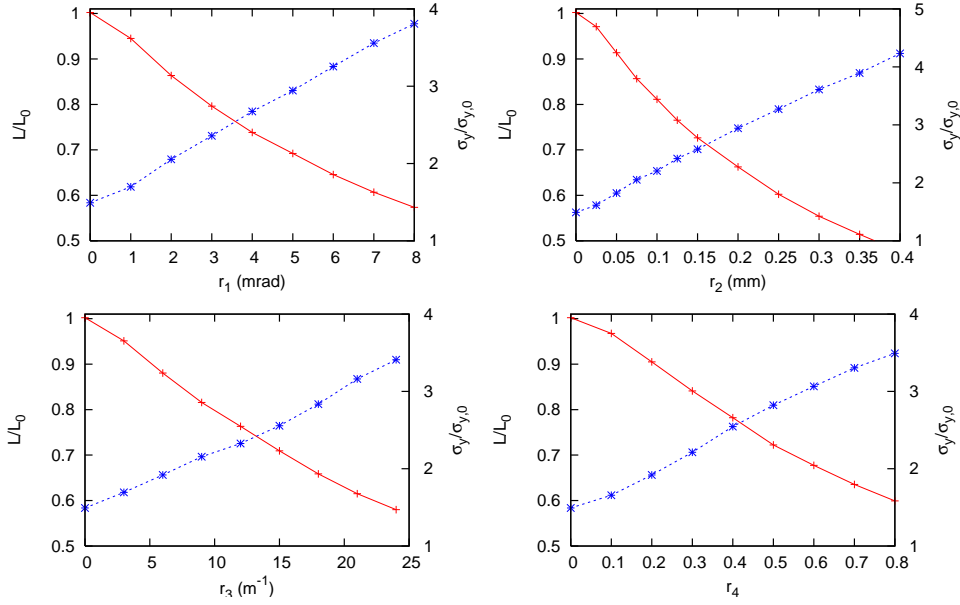
Figure 3.11: Luminosity and emittance degradations due to x-y coupling. Four pictures depict the degradations for $r_1 - r_4$. Red and blue lines are luminosity and beam size respectively.
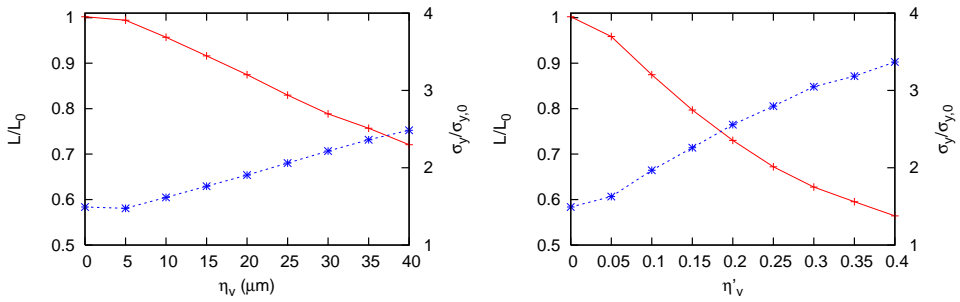


Figure 3.12: Luminosity degradation due to vertical dispersion. Left and right pictures depict the degradations for $\eta_y$ and $\eta'_y$, respectively. Red and blue lines are luminosity and beam size respectively.

Table 3.1: Summary for error tolerance

| | SuperKEKB | KEKB |
|---|---|---|
| $dx/\sigma_x$ (static) | 0.8 | - |
| $dy/\sigma_y$ (static) | 0.8 | 0.4 |
| $dx/\sigma_x$ (fast) | 0.08 | - |
| $dy/\sigma_y$ (fast) | 0.09 | 0.025 |
| $ds$ | 0.07 mm | 2 mm |
| $r_1$ | 3.0 mrad | 2.1 mrad |
| $r_2$ | 0.1 mm | 0.4 mm |
| $r_3$ | 10 m$^{-1}$ | 0.35 m$^{-1}$ |
| $r_4$ | 0.4 rad | 0.07 rad |
| $dr_1/d\delta$ | 2.1 | 6.1 |
| $dr_2/d\delta$ | 0.074 m | 2.5 |
| $dr_3/d\delta$ | 8400 m$^{-1}$ | 1100 m$^{-1}$ |
| $dr_4/d\delta$ | 290 | 440 |
| $\eta_y$ | 31 $\mu$m | 500 $\mu$m |
| $\eta_y'$ | 0.23 | 0.6 |

the perturbation maps for the chromatic aberrations. In that method, the momentum-dependent lattice nonlinearities are lumped to the IP.

The green dashed lines in Fig. 3.6 indicate the results using the SAD code. It is seen that the lattice nonlinearity enhances the synchro-betatron resonances by widening their widths. On the other hand, direct emittance growth and significant luminosity degradation are also observed from simulations. Due to these synchro-betatron resonances, the horizontal tunes of SuperKEKB are hard to be more closer to the half integer, as has been achieved in KEKB.

The luminosity performance as a function of bunch current products are shown in Fig. 3.13. In the figure, the red solid lines indicate results using the pure weak-strong model. The blue dashed lines indicates results using the weak-strong model plus perturbations of chromatic aberrations. The green dashed lines indicates results using the SAD code with the weak-strong model. The cyan lines represent the design values of luminosity and beam current products. It is seen that remarkable loss of luminosity appears at high bunch currents due to interplay of beam-beam and lattice nonlinearity in the LER. Especially, the specific luminosity drops quickly at very low beam currents. These phenomena can not be explained by the momentum-dependent

lattice nonlinearity. Dedicated analysis of the lattice nonlinearity in the LER are necessary to understand the mechanism. One possibility is that amplitude-dependent nonlinearities plays an important role in the LER. On the other hand, the luminosity loss due to interplay of beam-beam and lattice nonlinearity in the HER is not as serious as in the LER, and can be well attributed to the chromatic aberrations in the HER lattice.
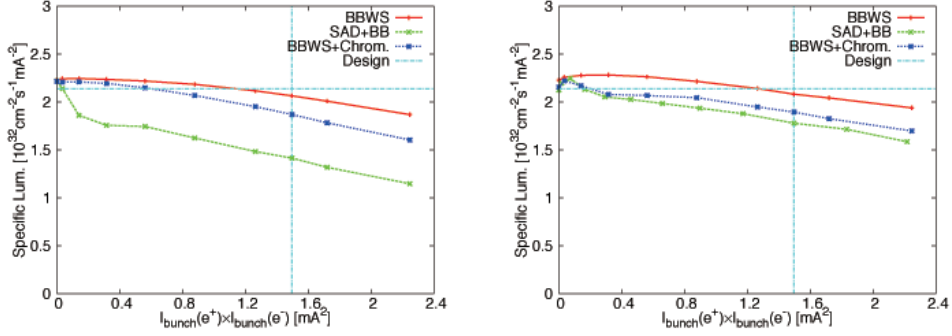


Figure 3.13: Specific luminosity as a function of bunch current products. Left picture is for LER, and right picture is for HER.

To further illustrate how lattice nonlinearity interplays with beam-beam interaction, frequency map analysis (FMA) is performed for three cases: bare lattice, pure beam-beam, and beam-beam with lattice nonlineairity. The initial conditions are taken over a mesh in the horizontal (x) and vertical direction (y) inside an area of $10\sigma_x \times 10\sigma_y$, and the corresponding tune footprints are plotted in the tune plane. The color indicates the diffusion rate of the particle motion. Figures 3.14 and 3.15 show the FMA results for LER and HER, respectively. In each figure, the blue dots extended from the origin (.53, .57) indicate footprints for a bare lattice; the black dots indicate footprints for pure beam-beam; the rest dots represent footprints for beam-beam with lattice nonlinearity. In the same figures, resonance lines up to eighth order are also plotted for reference.

From the frequency maps, the footprints in tune space with the bare lattice show strong dependence on initial amplitude. This is the results of strong amplitude-dependent lattice nonlinearity in both rings. The pure beam-beam interaction causes large spread in the vertical tunes while very small spread in the horizontal tune. The footprints are strongly deteriorated by the interplay between lattice nonlinearity and beam-beam. Particle with initial amplitudes of several sigmas performs very chaotic motion with large diffusion rate. The resonances driven by beam-beam are not clearly seen when lattice nonlinearity is included, because the particle motions become strongly chaotic.
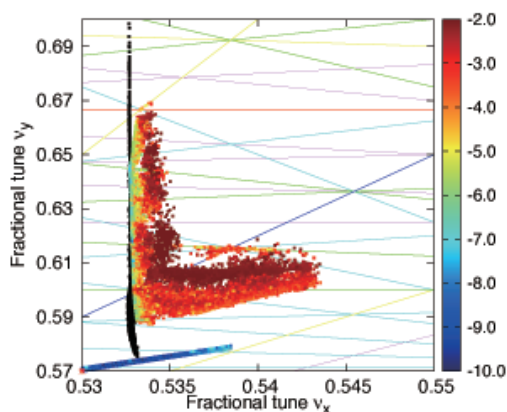
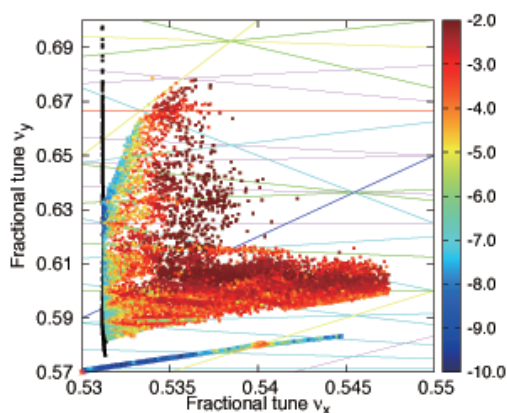Figure 3.14: FMA plot for the LER in the plane of betatron tunes.



Figure 3.15: FMA plot for the HER in the plane of betatron tunes.

### 3.1.7 Space charge

The first-order space-charge tune shift experienced by particles performing small oscillations around the beam centroid in a uncoupled lattice and for a gaussian bunch can be estimated by

$$\Delta\nu_i = -\frac{1}{4\pi}\frac{2r_e}{\beta^2\gamma^3}\int_0^C \frac{\lambda\beta_i}{\sigma_i(\sigma_x+\sigma_y)}ds \tag{3.13}$$

with $\beta_x$, $\beta_y$ are the beta functions, $\sigma_x$, $\sigma_y$ are the horizontal and vertical rms beam sizes, and $i = x, y$. The the longitudinal peak density is $\lambda(s) = N/\sqrt{2\pi}\sigma_z(s)$ with gaussian bunch profile assumed. In the case of SuperKEKB, the bunch length $\sigma_z$ is almost constant in the rings and we can ignore s-dependence of $\lambda$. In the absence of linear coupling, the horizontal beam sizes are calculated from emittance via $\sigma_x^2 = \epsilon_x\beta_x + \langle\delta^2\rangle D^2$ with $D$ the dispersion.

With design bunch populations, the estimated linear space-charge tune shifts are $\Delta\nu_x = -0.003$, $\Delta\nu_y = -0.087$ for LER, and $\Delta\nu_x = -0.0004$, $\Delta\nu_y = -0.012$ for LER. The tune shifts are rather small in HER, but the vertical tune shift in LER has the

same order as beam-beam tune shift with the opposite signs. The rms beam sizes and tune shift in the vertical plane along the LER lattice are plotted in Fig.3.16.
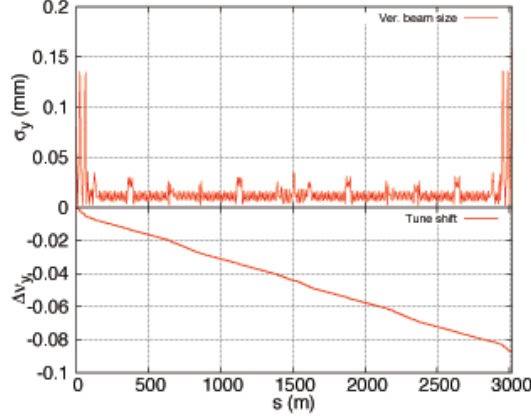


Figure 3.16: rms beam sizes and space charge tune shift in the vertical plane along the LER.

Similar to the beam-beam interaction, the space-charge force is highly nonlinear, and depends on the betatron amplitudes. Consequently, the footprints in the tune space may be distorted with the interplay of beam-beam, lattice nonlinearity and space charge. The influence of space-charge on luminosity performance is to be studied carefully via tracking simulations.

## 3.2 Electron Cloud effects

### 3.2.1 Electron cloud build up

Electrons, which is produced by photo-emission and secondary emission, are buit up in the positron ring, LER. To protect electrons, antechamber is adopted for the vacuum pipe. Synchrotron light hits the antechamber slot. Most of electrons do not come the central part of the chamber, where positron beam passes through. The electron cloud build up is evaluated by a simulation [4]. Primary electron is produced with the quantum efficiency 0.1 per photon incidence. The secondary electron is produced with the formula [5],

$$\delta_2(E) = \delta_{2,max} \times \frac{E}{E_{max}} \frac{1.44}{0.44 + (E/E_{max})^{1.44}}, \tag{3.14}$$

where $\delta_{max} = 1.2$ at $E_{max} = 300$ eV.

Figure 3.17 shows the electron cloud distribution and density in the antechamber. The electron density near the beam is obtained as $2.2 \times 10^{11}$ m$^{-3}$. As is shown later, the density is critical for both of the coupled and single bunch instabilities. The density is reduced one order magnitude by groove structure and weak solenoid magnets.
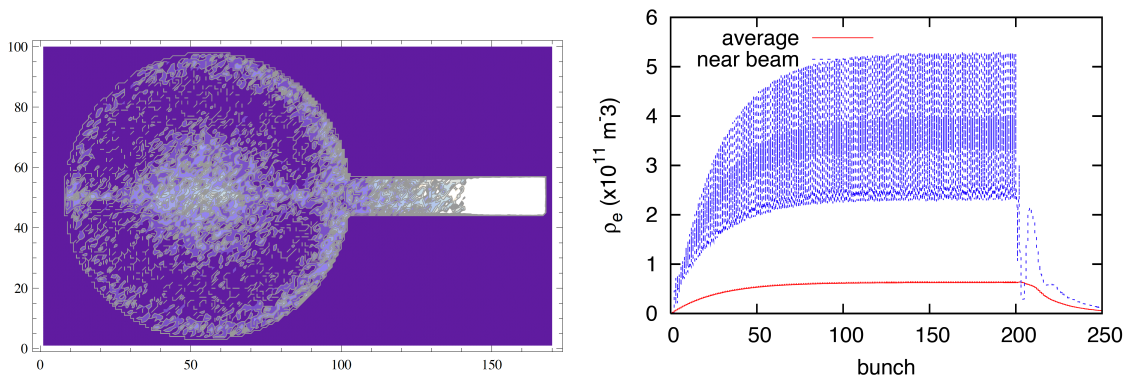
<center>54</center>

Figure 3.17: Electron cloud distribution and buildup in antechamber.

## 3.2.2    Coupled bunch instability

Bunch train experiences a long range ($\sim$ 10 ns) wake field due to the electron cloud. A coupled bunch instability is caused by the wake field [6]. Figure 3.18 shows the wake field and growth rate of the instability. The fastest growth is the mode number $\sim$ 2000 and its rate is 0.025 (40 turns). This growth rate is comparable with the feedback damping time. Since the electron cloud is reduced further 1/2-1/10, this coupled bunch instability is manageable.
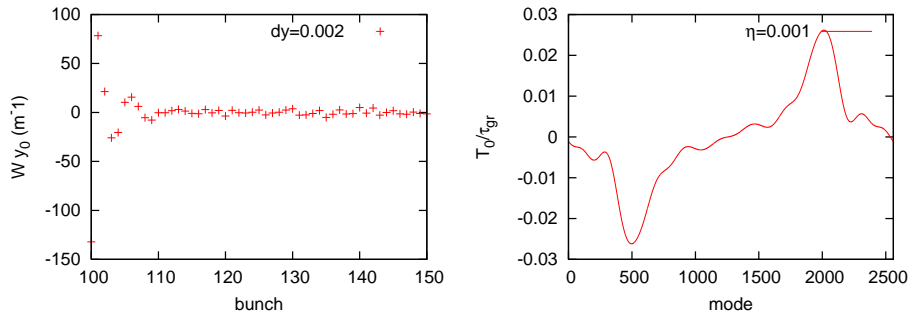


Figure 3.18: Wake field and growth rate for electron cloud induced coupled bunch instability.

### 3.2.3   Single bunch instability

**constant beta**

As the first step, the estimation of single bunch instability is performed in the condition that electon cloud distributes uniformly along the ring and the beta function is constant. Electrons oscillate in the electric potential formed by the positron bunch. The frequency is expressed by

$$\omega_e = \sqrt{\frac{\lambda_p r_e c^2}{\sigma_y(\sigma_x + \sigma_y)}}, \tag{3.15}$$

where $\lambda_p$ is the local line density of the positron bunch. The frequency is 10-100 GHz in typical positron rings. The electrons oscillate several period during the passage of a positron bunch. The oscillation induces a short range wake field with the frequency, $\omega_e$. Fast head tail instability is caused by the wake field. Horizontal motion is slower than vertical one, thus vertical motion is more serious for the instability. The threshold of the vertical single bunch (fast head-tail) instability is given by

$$\rho_{e,th} = \frac{2\gamma\nu_s\omega_e\sigma_z/c}{\sqrt{3}KQr_e\beta_y L}, \tag{3.16}$$

where $K = \omega_e\sigma_z/c$ and $Q = min(\omega_e\sigma_z/c, 10)$ are used.

Tables 3.2 and 3.3 show parameters and threshold electron density of positron rings, in which electron cloud effect is/should be observed. The threshold is $2.7 \times 10^{11}$ m$^{-3}$ for SuperKEKB.

The single bunch instability is simulated by solving beam-electron cloud interactions. The simulation is performed by the same method as the strong-strong beam-beam simulation. A bunch is sliced into many pieces ($> \omega_e\sigma_z/c$). Interaction between a bunch slice and electron cloud is evaluated by potential solver based on the particle in cell method. The synchrotron radiation damping and excitation are not taken into account to be clear the instability threshold in this subsection. The radiation damping/excitation is taken into account in Sec. 3.2.4 to evaluate equilibrium emittance.

Figure 3.19 shows evolution of the vertical beam size and a snapshot of beam-electron motion. The threshold density is $3.8 \times 10^{11}$ m$^{-3}$ as shown in left picture. Right picture depicts motion of bunch slices and electron centroid during the interaction for $\rho_e = 4.2 \times 10^{11}$ m$^{-3}$ at 4000-th turn. Coherent motion of bunch slices and electron cloud is seen.

In the threshold estimation, $\beta_y = 10$ m is used as a typical value. Eq.(3.17) informs threshold of $\int \rho_e\beta_y ds$: i.e. lower threshold for higher beta. This is true if the dynamics

Table 3.2: Basic parameters of the positron rings

| Lattice | | KEKB | Cesr-TA | PETRA-III | SuperKEKB | Super B |
|---|---|---|---|---|---|---|
| Circumference | $L$ (m) | 3,016 | 768 | 2304 | 3016 | 1260 |
| Energy | $E$ (GeV) | 3.5 | 2-5 | 6 | 4.0 | 6.7 |
| Bunch population | $N_+(10^{10})$ | 8 | 2 | 0.5 | 9 | 5 |
| Beam current | $I_+$ (A) | 1.7 | - | 0.1 | 3.6 | 1.9 |
| Emittance | $\varepsilon_x$(nm) | 18 | 2.3 | 1 | 3.2 | 2 |
| | $\varepsilon_y$(nm) | 0.18 | 0.023 | 0.01 | 0.01 | 0.005 |
| Momentum compaction | $\alpha(10^{-4})$ | 3.4 | 68 | 12.2 | 3.5 | |
| Bunch length | $\sigma_z$(mm) | 6 | 6.8 | 12 | 6 | 5 |
| RMS energy spread | $\sigma_E/E(10^{-3})$ | 0.73 | 0.8 | | 0.8 | 0.64 |
| Synchrotron tune | $\nu_s$ | 0.025 | 0.067 | 0.049 | 0.0256 | 0.0126 |
| Damping time | $\tau_x$(ms) | 40 | 56.4 | 16 | 43 | 26 |
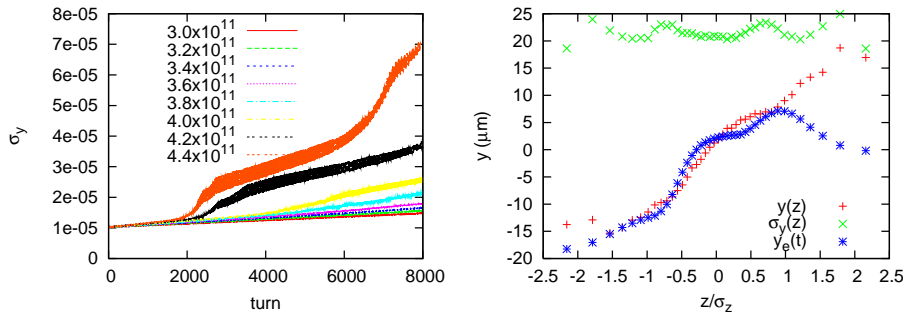


Figure 3.19: Evolution of the vertical beam size for various electron cloud density (left) and motions of bunch slices and electron centroid (right).

Table 3.3: Threshold of electron cloud density in positron rings.

| | | KEKB (no sol.) | KEKB (50 G sol.) | Cesr-TA | PETRA-III | SuperKEKB | SuperB |
|---|---|---|---|---|---|---|---|
| Bunch population | $N_+(10^{10})$ | 3 | 8 | 2 | | 8 | 5 |
| Beam current | $I_+$ (A) | 0.5 | 1.7 | - | 0.1 | 3.6 | 1.9 |
| Bunch spacing | $\ell_{sp}$(ns) | 8 | 7 | 4-14 | 8 | 4 | 4 |
| Electron frequency | $\omega_e/2\pi$(GHz) | 28 | 40 | 43 | 35 | 150 | 175 |
| Phase angle | $\omega_e\sigma_z/c$ | 3.6 | 5.9 | 11.0 | 8.8 | 18.8 | 18.3 |
| Threshold | $\rho_e$ ($10^{12}$ m$^{-3}$) | 0.63 | 0.38 | 1.7 | 1.2 | 0.27 | 0.54 |

of the beam-electron cloud do not change. The threshold is obtained as

$$\oint \rho_e\beta_y ds = 27(\text{formula}) - 38(\text{simulation}) \times 10^{12} \text{ m}^{-1}. \tag{3.17}$$

These threshold values are critical for the electron build-up estimation without special cures in Figure 3.17.

**realistic beta and cloud density**

The beam-electron cloud interaction depends on the local electron density and beam size. The frequency of electrons $\omega_e$ in Eq.(3.15) depends on $s$, because of the beam size variation. $\beta_y$ gives coupling between beam-electron interaction as shown in Eq.(3.16). The tune shift caused by the electron clouds is expressed as

$$\Delta\nu_y = \frac{r_e}{k\gamma}\rho_e\beta_y, \tag{3.18}$$

where $k = 1$ or 2 for flat or round electron distributions, respectively.

The vacuum group estimates electron density profile along $s$. Figure 3.20 shows the variation of $\beta_{x,y}$ and $\rho_e$. The density is around $0.2 \times 10^{11}$ m$^{-3}$ in most of the sections as shown in left picture. It is high at the symmetric point for IR. The density near IR is depicted in the right picture. Very high $\beta$ and dispersive sections are located near IR ($s = 27$ and 68 m) for the local chromaticity correction. Bending magnets are located in the sections. Single bunch instability and nonlinear emittance growth are studied in two cases; (1) electron is suppressed (green) and (2) is not suppressed (cyan) at the high beta sections.

Figure 3.21 shows $\int_0^s \rho_e\beta ds$ and the vertical tune shift along the ring for the two cases. Tune shift, which arises in arc the section, is 0.0003, while that in IR is 0.0012 or 0.0009 for case (1) or (2), respectively. In either case, the tune shift in IR is dominant.

Figure 3.22 shows electron oscillation phase $\omega_e \sigma_z/c$. The electron oscillation is 20 in arc, while is 5 or less in IR. The variation of $\omega_e$ reduces the quality factor of the wake force induced by electron cloud.
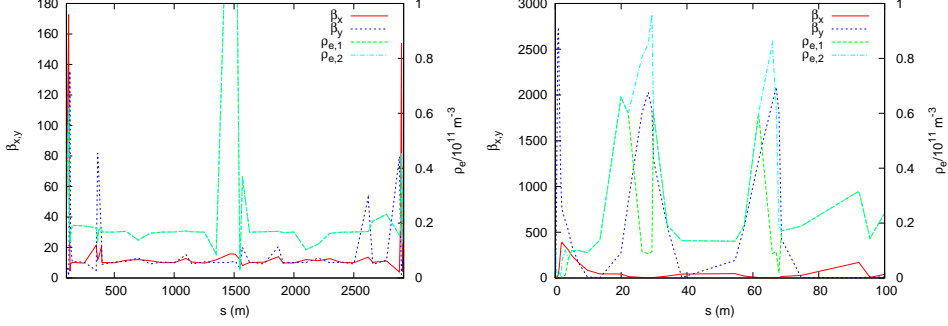


Figure 3.20: $\beta_y$ and electron central density $\rho_e$ along $s$. Left and right pictures depict whole ring and IR area, respectively.
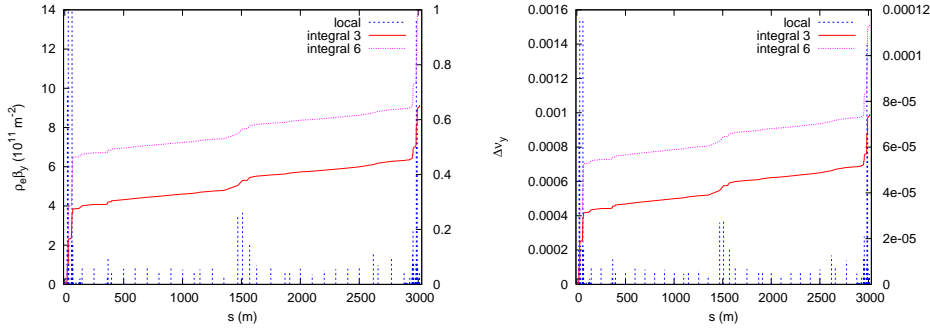


Figure 3.21: $\int_0^s \rho_e \beta ds$ and the vertical tune shift along the ring.

Figure 3.23 shows the evolution of the vertical beam size for various electron cloud density. The density at symmetry point ($s = 1500$ m) is written in the pictures. The design cloud density is $10^{11}$ m$^{-3}$ at $s = 1500$ m. The density distributes along $s$ as shown in Fig. 3.20.

Left and right pictures depict beam size evolution for the cases (1) and (2), respectively. The threshold is $6\times$ or $4\times$ of the design for the cases (1) and (2), respectively.

We investigate which electron clouds in arc or IR is dominant for the instability. Figure 3.24 shows instability threshold caused by electron cloud in IR (left picture) or arc (right picture). The threshold density is $4 - 5\times$ or $20\times$ of the design for electrons only in IR or only in arc, respectively. The electron cloud distribution of the case (2) is examined. The contribution of $\int \rho \beta_y ds$ is 4:1 as shown in Fig.3.21. The threshold densities are consistent with the ratio of $\int \rho \beta_y ds$.
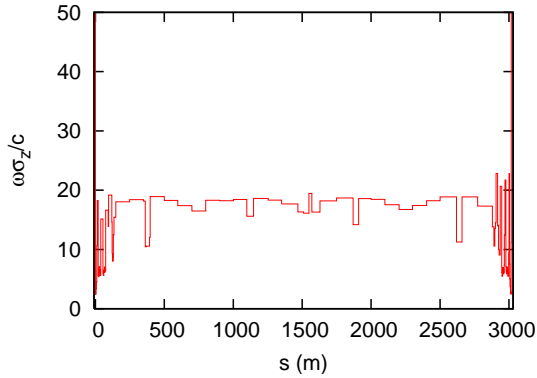
Figure 3.22: Variation of electron oscillation phase $\omega_e \sigma_z/c$.
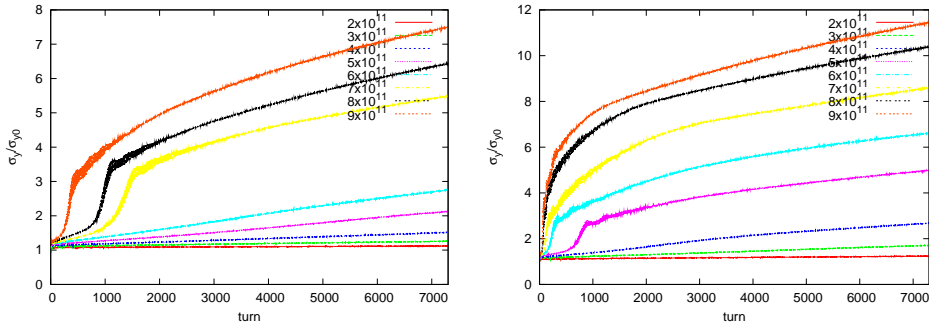


Figure 3.23: Evolution of the vertical beam size for various electron cloud density. The relative density distribution is given in Fig. 3.20.
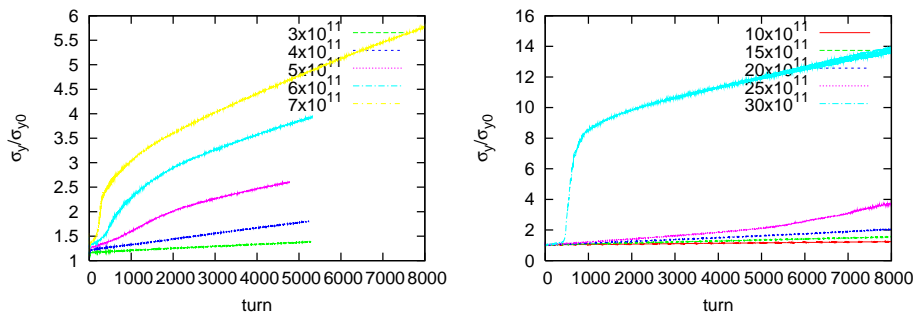


Figure 3.24: Evolution of the vertical beam size for various electron cloud density. In the left picture, electrons distribute only in IR, $s < 75$ and $s > 2940$ m. In the right picture, electrons distribute only in arc section, $75 < s < 2940$ m. The electron cloud distribution is the case (2).

### 3.2.4 Nonlinear emittance growth

Emittance growth is seen bellow the threshold of the fast head-tail instability in Figures 3.23 and 3.24. The emittance growth is caused by nonlinear force due to the electron cloud charge distribution. In the simulation, particles are tracked with a large time step $\Delta s > \beta_y$ in arc section, while with a short time step $\Delta s < \beta_y$. Emittance growth caused by electron in IR can be predicted accurately. The tune shift contribution is dominant in IR. Figure 3.25 shows the variation of $\beta_y$ and its phase in IR section. Locations with very high $\beta_y$ are separated with the phase $\pi$. Since electron transverse distribution is considered to be symmetric for $y$, the nonlinear effect is accumurated every high $\beta_y$ locations.
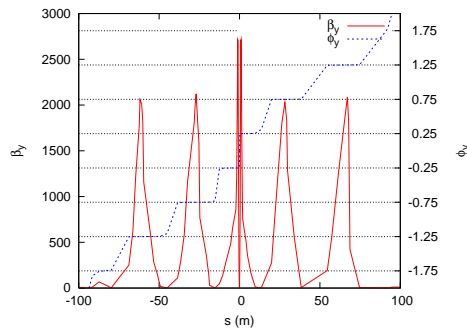


Figure 3.25: Vertical beta function and betatron phase variations in IR section.

To evaluate equilibrium emittance for the nonlinear growth, the radiation damping and excitation is taken into account in the simulation. Figure 3.26 shows evolution of the vertical beam size with (green) and without radiation damping/excitation. The vertical radiation damping time is 4300 turns. The equilibrium emittance is realized after around 9000 turns.

Figure 3.27 shows the evolutions of the vertical beam size for various electron density. Left and right pictures depict the evolutions for the cases (1) and (2). The equilibrium beam size is obtained as functions of the electron density. In the right picture, beam size evolutions above the threshold ($\rho_e = 3\times$ design) with and without synchrotron damping/excitation are plotted. We find that the radiation damping somewhat suppresses the coherent single bunch instability.

Figure 3.28 shows the equilibrium emittance as function of electron density. The emittance increase is not serious for the design cloud density, but become serious 3 times or more.
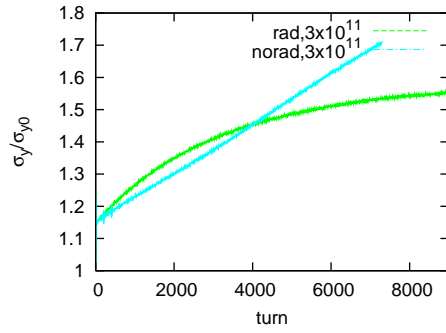
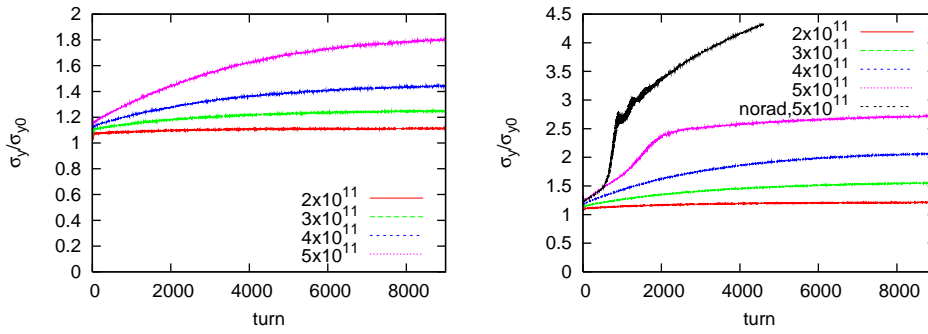Figure 3.26: Evolution of the vertical beam size with (green) and without (cyan) radiation damping/excitation.



Figure 3.27: Evolution of the vertical beam size for various electron density. Left and right pictures depict the evolutions for the cases (1) and (2).
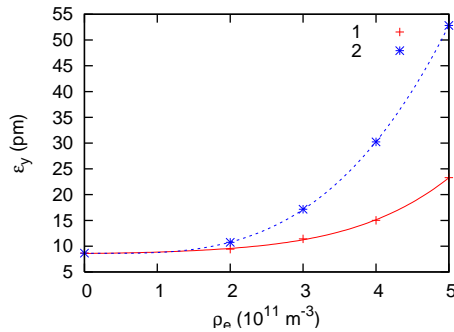


Figure 3.28: Equilibrium emittance as functions of the electron cloud density. Two lines, red and blue, are drawn for the cases (1) and (2), respectively.

### 3.2.5 Summary

Conclusions for the electron cloud effects are summarized in the following.

- The vacuum system is designed so that electron density near the beam is suppressed around $\rho_e = 1 \times 10^{11}$ m$^{-3}$ at the peak ($s = 1500$ m) and $2 \times 10^{10}$ m$^{-3}$ in average of whole ring.

- The growth time of the coupled bunch instability is about 400 turn and is manageable.

- The threshold electron density is 4-6 times higher than that of the design value.

- Electrons near IR are dominant sources for the instability.

- The emittance growth is negligible for $\rho_e \leq 2 \times$ design value.

# Bibliography

[1] http://acc-physics.kek.jp/SAD/sad.html.

[2] D. Zhou, K. Ohmi, Y. Seimiya, Y. Ohnishi, A. Morita and H. Koiso, Phys. Rev. ST Accel. Beams **13**, 021001 (2010).

[3] Y. Seimiya, K. Ohmi, D. Zhou, J. W. Flanagan and Y. Ohnishi, Progress of Theoretical Physics **127**, 1099 (2012).

[4] K. Ohmi, Phys Rev. Lett. 75, 1526 (1995).

[5] M.A. Furman, G.R.Lambertson, Proceedings of MBI97 (KEK-report No.97-17), p.170.

[6] K. Ohmi, F. Zimmermann, Phys. Rev. Lett. 85, 3821 (2000).